

An analysis of interdecadal variations in the perturbational feedback parameter based on a MIROC6 piControl simulation

Ko Tsuchida (✉ tsuchida.kou.070@s.kyushu-u.ac.jp)

Kyushu University: Kyushu Daigaku <https://orcid.org/0000-0001-8605-0233>

Takashi Mochizuki

Kyushu University: Kyushu Daigaku

Ryuichi Kawamura

Kyushu University: Kyushu Daigaku

Tetsuya Kawano

Kyushu University: Kyushu Daigaku

Research Article

Keywords: Climate sensitivity, Internal variation, ENSO, Background field, Decadal variation

Posted Date: September 16th, 2021

DOI: <https://doi.org/10.21203/rs.3.rs-904989/v1>

License:  This work is licensed under a Creative Commons Attribution 4.0 International License.

[Read Full License](#)

38 **Keywords:** Climate sensitivity, Internal variation, ENSO, Background field, Decadal variation

39 1. Introduction

40 Understanding the climate response to external forcing, such as anthropogenic forcing, is crucially
41 important for projecting and evaluating the future climate. The concept of climate sensitivity relates to how the
42 climate system responds to external forcing, such as greenhouse gases and aerosols. Equilibrium climate sensitivity
43 (ECS) is one of the most widely used forms of climate sensitivity, and it is defined as the change in the steady-
44 state global-mean surface air temperature that will eventually occur in relation to a doubling of the CO₂
45 concentration. ECS is not only applied in IPCC, but it is also a convenient indicator used to compare the climate
46 system responses of several general circulation models (GCMs) (Kunutti and Hegerl 2008; Andrews et al. 2012;
47 Gregory et al. 2020).

48 Processes in a climate system that can either amplify or dampen the climate system response to an external
49 perturbation are referred to as climate feedback (Bony et al. 2006). In estimating the values of climate sensitivity
50 and climate feedback, a simplified energy balance concept is generally used, as shown by the equation below,

51
52
$$N = F - R = F - \alpha T, \quad (1 - 1)$$

53
54 where N is the net downward radiation flux (positive downward) change at the top of the atmosphere [W/m^2],
55 F is the external forcing [W/m^2] affecting the climate system (positive downward), R is the climate radiative
56 response [W/m^2] connected to the change in surface temperature T [K] (positive upward), and α is the climate
57 feedback parameter [$\text{W}/\text{m}^2/\text{K}$] (Gregory et al. 2004; Gregory and Webb 2008). Therefore, a precise estimation
58 of α is a central parameter required in the quest to understand the global warming tendency.

59 ECS is derived by taking advantage of $N = 0$, which is apparent from its definition. Therefore, if α is
60 already known, ECS can be expressed as

61
62
$$ECS = \frac{F_{2\times}}{\alpha} = sF_{2\times}, \quad (1 - 2)$$

63
64 where $F_{2\times}$ is the radiative forcing due to a doubling of the CO₂ concentration, and s is the effective climate
65 sensitivity parameter [$\text{K}/\text{W}/\text{m}^2$]. As the climate feedback parameter α increases, negative feedback increases,
66 and the system becomes more stable.

67 In this respect, uncertainty in estimating the value of α is primarily due to the framework of climate models,
68 such as the implemented calculation schemes for clouds. In addition, ECS cannot be directly estimated when using
69 the climate system in historical experiments or in the ScenarioMIP experiment, as these are not considered to be
70 in equilibrium states. In practice, α is estimated from climate fluctuations, and it is thus dependent on the climate
71 state of the period in focus (Gregory et al. 2002; Gregory et al. 2004; Forster and Gregory 2006; Tett et al. 2006;
72 Otto et al. 2013). As α cannot be obtained as a constant value, it is referred to as effective climate sensitivity
73 (EffCS) (Senior and Mitchell 2000; Gregory et al. 2002), which is dependent on environmental states. The time

74 dependency of α has recently attracted attention as an important source of uncertainty in projecting the warming
75 rate of future climates. Furthermore, when using certain climate models, ensembles of historical simulations result
76 in large uncertainties when estimating α (Watanabe et al. 2021), which indicates the possibility that internal
77 variability also plays an important role in climate feedback variation.

78 Recently, Gregory and Andrews (2016) examined the time changes of α by introducing the feedback
79 parameter variation. They achieved this by applying the parameter defined in Gregory et al. (2004), which is as
80 follows,

81

$$82 \quad \tilde{\alpha} = -\frac{dN}{dT}, \quad (1 - 3)$$

83

84 where $\tilde{\alpha}$ is known as the differential feedback parameter (DFP), and its value is defined by the slope of the
85 ordinary least squares (OLS) regression of the annual means of N against T over 30 years. They also estimated
86 the DFP value in atmospheric general circulation model simulations (AGCM, Had GEM2, and HadCM3 in their
87 study) using observed SST and sea ice with preindustrial forcing ($F = 0$, which is referred to as the amipPIForcing
88 experiment). The DFP from the model ensembles was an average of $1.7 \text{ W/m}^2/\text{K}$, and the results also provided
89 interdecadal variations. The study revealed that the main control of DFP variations was changes in the SST trend
90 pattern. The results of another study using other CMIP5 models also showed similar interdecadal DFP variability
91 (Andrews et al. 2018).

92 The observed SST trend pattern change in Gregory and Andrews (2016) is composed of externally
93 forced variability and internal variability on annual to interdecadal timescales. However, further investigations of
94 the internal variability of DFP and deriving an accurate evaluation of this would enable verification of the role of
95 internal variability in climate feedback variation and its physical mechanism in atmosphere-ocean coupling
96 systems. In addition, refining climate feedback estimations would improve near-future climate predictions, in
97 which both trends of internal variability and global warming play important roles. Therefore, this study defines a
98 new feedback parameter to determine the influence of internal variability in relation to variations in DFP, and then
99 clarifies its mechanism.

100 The aims of this study are as follows: to demonstrate the interdecadal variability of climate feedback by
101 proposing a new feedback parameter, known as the Perturbational Feedback Parameter (PFP); to identify changes
102 in the background field that are closely connected to variations in the parameter; and to clarify the mechanism
103 involved in feedback variability, with a particular focus on the contributions from annual and interannual variations
104 that dominate under the background states.

105 The remainder of this paper is organized as follows. Section 2 describes the materials and methods used,
106 with a particular emphasis on defining the PFP. The properties of the PFP and the features in the background field
107 that are deeply connected to PFP variations are provided in Section 3. The changes in annual and interannual
108 variations in relation to the background changes and their contribution to PFP variations are also clarified. Section
109 4 discusses the results and presents the main conclusions.

110
111
112
113
114
115
116
117
118
119
120
121
122
123
124
125
126
127
128
129
130
131
132
133
134
135
136
137
138
139
140
141
142
143
144
145

2. Materials and methods

2.1 Data

We analyzed the simulation results from the 6th version of the Model for Interdisciplinary Research on Climate (MIROC6), which contributed to CMIP6 (Tatebe et al. 2019). The "piControl simulation," simulates atmospheric and oceanic interdecadal variation over 800 years (3200–3999, virtual years from the simulation start) by keeping the atmospheric forcing components constant in the preindustrial state, and the following data were obtained from the simulation: surface temperature(ts), downward shortwave radiation flux at TOA (rsdt, TOA: top of atmosphere), upward shortwave radiation flux at TOA (rsut), upward longwave radiation flux at TOA (rlut), clear-sky upward shortwave radiation flux at TOA (rsutcs), clear-sky upward longwave radiation flux at TOA (rlutcs), mass fraction of cloud water (clw), mass fraction of cloud ice (cli), zonal wind (ua), meridional wind (va), vertical wind (wap), atmospheric temperature (ta), and seawater temperature (thetao). The horizontal resolution of the model data was $1.4^\circ \times 1.4^\circ$ (for seawater temperature, $0.5\text{--}1^\circ \times 1^\circ$), and the vertical resolution was as follows: 19 layers (from 1000 hPa to 1 hPa) for ua, va, and wap; 81 layers for clw, cli, and ta (surface to 0.004 hPa by using a hybrid $\sigma - p$ coordinate; Arakawa and Konor (1996) for the purpose of reproducing stratospheric circulation); and 62 layers (sea surface to the sea bottom by using a hybrid $\sigma - z$ coordinate) for thetao (49 layers for tropics). The annual mean data derived from monthly mean data were analyzed in this study.

2.2 Definition of PFP (Perturbational Feedback Parameter)

In this section, we define the perturbational feedback parameter (PFP), α , with the aim of enabling an investigation of the interdecadal variations in the strength of climate feedback associated with internally generated climate variability.

The values of the PFP are defined as the linear regression coefficient obtained from the relation between the global-mean anomalies of the net downward radiation flux at the top of the atmosphere, N' , and those of surface temperature, T' , within a 30-year window (Gregory and Andrews 2016),

$$\alpha = -\frac{\Delta N'}{\Delta T'}. \tag{2-1}$$

It is of note that the anomalies deviate from the climatology of 800-year-long simulations and that the PFP is derived by inverting the sign as in Gregory and Andrews (2016). From this definition, the PFP indicates how the global mean net downward radiation flux changes according to a rise in the global mean surface temperature, and negative feedback increases when the PFP is larger.

The temporal evolution of the PFP value is first defined, and the physical mechanism controlling PFP variations is then clarified by focusing on changes in the interannual fluctuations and mean states within 30-year windows.

146
 147
 148
 149
 150
 151
 152
 153
 154
 155
 156
 157
 158
 159
 160
 161
 162
 163
 164
 165
 166
 167
 168
 169
 170
 171
 172
 173
 174
 175
 176
 177
 178
 179
 180

2.3 Modified Regression Value

In this section, we define a modified regression value in detecting predominant fluctuations that characterize PFP variations, used in 3.3. In calculating the regression values with the area-averaged SST fluctuations (i.e., Nino3.4 SST or the northeastern Pacific SST shown in Figures 3c), we introduced a scaling factor, which is defined as the regression of area-averaged SST with global-mean surface temperature fluctuations. In other words, we examined the product of a specific fluctuation at each grid point regressed onto the area-averaged SST and the area-averaged SST regressed onto the global-mean surface temperature. These scaled regression values enabled us to estimate the contribution to the global-mean fluctuation at each grid point through a specific climate mode represented by the fluctuation in area-averaged SST, and the following equations were employed,

Modified Regression value =

$$\frac{\sum(V_{local} - \bar{V}_{local})(T_{Nino3.4} - \bar{T}_{Nino3.4})}{\sum(T_{Nino3.4} - \bar{T}_{Nino3.4})^2} \times \frac{\sum(T_{Nino3.4} - \bar{T}_{Nino3.4})(T_{global} - \bar{T}_{global})}{\sum(T_{global} - \bar{T}_{global})^2}, \quad (2 - 2)$$

Modified Regression value =

$$\frac{\sum(V_{local} - \bar{V}_{local})(T_{NEP} - \bar{T}_{NEP})}{\sum(T_{NEP} - \bar{T}_{NEP})^2} \times \frac{\sum(T_{NEP} - \bar{T}_{NEP})(T_{global} - \bar{T}_{global})}{\sum(T_{global} - \bar{T}_{global})^2}, \quad (2 - 3)$$

where V_{local} is an arbitrary variable (in each grid point), T_{global} is the global mean surface temperature, $T_{Nino3.4}$ is Nino3.4 SST, T_{NEP} is northeastern Pacific SST, and the superscript bar shows the average data for either 424 years in PFP_large or 365 years in PFP_small.

3. Results

3.1 PFP variations and associated properties

Although external forcing was fixed in the 800-year-long simulation, values of PFP showed interdecadal variations (Figure 1), and the average and standard deviation of its timeseries were 1.47 [W/m²/K] and 0.37 [W/m²], respectively.

Interdecadal variations in PFP were accompanied by large-scale climate variability within the 30-year running mean states (Figure 2). Figure 2a shows a correlation map between the 30-year running mean surface temperature and PFP variations. When the PFP was positive, the surface temperature increased over the equatorial Pacific and decreased over the western equatorial Pacific, and an east-west contrast was clearly evident. Consequently, the zonal SST contrast along the equator was weakened. Figure 2b shows the longitude-depth section of the 30-year running mean ocean-water temperature averaged over 5S-5N regressed onto the PFP. Corresponding to the SST changes, the subsurface ocean temperature weakened the zonal gradient of the ocean thermocline over the equatorial Pacific.

181 3.2 PFP variation with interannual variation

182 3.2.1 Fluctuations of surface temperature and net downward radiation flux within a 30-year window

183 Variations in both the surface temperature and net downward radiation flux were found to contribute to
184 PFP variation. We thus investigated the correlations between PFP variation and the standard deviations of global
185 mean surface temperature and net downward radiation flux within a 30-year window to determine which variable
186 provided the most dominant contribution. The results showed that the correlation between PFP and the standard
187 deviation of the global mean surface temperature was 0.52, whereas that of the net downward radiation flux was
188 0.76 (Figure 3a, b). This showed that the variation in PFP was mainly controlled by the variation width of the
189 global mean net downward radiation flux and not by surface temperature within a 30-year window.

190 It was then necessary to determine the area in which the global mean net downward radiation flux change
191 originated. Using the PFP time series, the regression maps of the standard deviations of local surface temperature
192 and net downward radiation flux were analyzed to provide insight into gaining an understanding of the physical
193 mechanism. Figure 3c shows a map of the standard deviation of surface temperature regressed onto the PFP, where
194 it is evident that deviations in the annual mean surface temperature over the equatorial Pacific increase when the
195 PFP is large. In addition, large signals are also found over the mid-latitudes of the northern Pacific and Alaska.

196 Figure 3d shows a map of the standard deviation of net downward radiation flux regressed onto the PFP,
197 where it is evident that deviations of annual net downward radiation flux over the equator and its north-south area
198 increase when the PFP is large. The PFP value is directly controlled by deviations in the global mean net downward
199 radiation flux over 30 years (Figure 3b), and it is mainly controlled by the equatorial and subtropical net downward
200 radiation flux amplitude in the Pacific (Figure 3d). However, PFP variation is less dependent on the global mean
201 surface temperature amplitude (Figure 3a), while it is related to the local surface temperature in the equatorial and
202 northeastern Pacific (Figure 3c). This suggests that changes in the surface temperature over the equatorial and
203 northeastern Pacific may drive net downward radiation flux changes over the tropical and subtropical Pacific via
204 atmospheric circulation and cloud changes.

205

206 3.2.2 Differences between the interannual variations of PFP_large and PFP_small

207 To clarify the physical mechanisms that control the statistical relationships between PFP and surface
208 temperature and net downward radiation flux, we conducted composite analyses based on the PFP values. The
209 PFP values that fluctuated in 30-year windows by over one standard deviation (in either positive or negative values)
210 were categorized as PFP_large and PFP_small, respectively, and the differences between these two categories
211 were discussed. In particular, we examined the sensitivity of surface temperature and net downward radiation flux
212 variations at each grid point to the variations in global-mean surface temperature, as its amplitude was less
213 dependent on the PFP values (Figure 3a).

214 PFP_large was thus defined as a PFP value larger than $1.85 \text{ [W/m}^2\text{/K]}$, which was the average PFP variation
215 plus one standard deviation of variation in 800 years, and PFP_small was defined as a PFP value less than
216 $1.11 \text{ [W/m}^2\text{/K]}$, which was the average PFP variation minus one standard deviation of variation in 800 years. A
217 total of 424 years and 365 years fell into each respective category. It is of note that although specific years in a 30-

218 year window of PFP_large could be concurrently counted in another 30-year window of PFP_small, this did not
219 disrupt our analysis because we used the results to analyze the statistical features of 30-year windows. The
220 regression difference from PFP_large to PFP_small was then analyzed.

221 Figure 4a shows a map of the differences between PFP_large and PFP_small when the local surface
222 temperature was regressed onto the global mean surface temperature anomaly. The result reveals an anomalous
223 warming of surface temperature in the eastern equatorial Pacific and an anomalous cooling in the extratropical
224 Pacific with a rise in the global mean surface temperature rise in PFP_large. Again, the positive values in the
225 tropical Pacific correspond to the intensification of the ENSO amplitude when the PFP value increases, as
226 mentioned in Section 4.1. Figure 4b shows a map of the difference between PFP_large and PFP_small when the
227 net downward radiative flux was regressed onto the global mean surface temperature. The result reveals an
228 anomalous net downward radiation flux in the northern part of the equator and an anomalous net upward radiation
229 flux in the subtropics and on the equator.

230 However, the signals in the net downward radiation flux in Figure 4a do not merely represent local
231 responses to the surface temperature fluctuations. Large regression differences are also found in the tropical Pacific,
232 which implies that significant changes occur in the Pacific ITCZ and the subtropical Pacific rather than in the mid-
233 and high latitudes. We thus focus on the tropical and subtropical Pacific areas to conduct the following analyses.

234 The difference in the regression value of net downward radiative flux in Figure 4b correlates well with that
235 of the cloud distribution. Figure 5a and 5b are maps of the differences between the cloud water contents of
236 PFP_large and PFP_small in the low and middle troposphere, respectively, regressed onto the PFP, which were
237 derived using the same method as that used to obtain the results shown in Figure 4a and 4b. Low-level clouds
238 showed anomalous positive values in the subtropical Pacific Ocean (Figure 5a). Figure 5b shows that middle-level
239 clouds have anomalous negative values in the northern part of the tropical Pacific and positive values along the
240 equatorial Pacific, and these changes in clouds may be comparable to those of the net downward radiative flux
241 (Figure 4b).

242 Figure 6 shows the meridional circulation of the atmosphere, air temperature, and the mass content of cloud
243 water that were zonally averaged in the eastern tropical and subtropical Pacific (shown in Figure 4a, 30S-30N)
244 where the regression values relate to large differences in surface temperature (Figure 4a). There is an ascending
245 flow anomaly (positive value of the regression difference) on the equator and a descending flow anomaly (negative
246 value of the regression difference) in the subtropics, and this enhances the Hadley circulation when the PFP value
247 is large (Figure 6a).

248 Consistent with the enhanced convective activity along the equator, there is a warming anomaly (positive
249 regression value difference) in the middle to upper layers and the lower layers on the equator (Figure 6b). The
250 cloud water content increases and decreases, particularly in the middle layer over the equatorial and off-equatorial
251 areas, respectively (Figure 6c), which suggests that the convective activity is concentrated in a narrow area along
252 the equator. In addition, there is a cooling anomaly (negative value of regression difference) in the lower layers of
253 the subtropics (Figure 6b), where descending flow prevails (Figure 6a) and cloud water content above the layers
254 increases (Figure 6c).

255 3.3 Predominant fluctuations characterizing PFP variation

256 It has been revealed that the strengthening of ascending flow on the equator due to surface temperature rise
257 in the eastern Pacific and the descending flow in the subtropics due to the enhanced static stability causes changes
258 in the amount and distribution of cloud, and thus changes in net downward radiation change. Although these
259 variations are superposed by multiple timescale fluctuations, it is uncertain which timescale fluctuations are
260 dominant in characterizing the aforementioned variations.

261 The Nino3.4 index (SST anomaly averaged over 5S-5N, 170 W-120W, blue rectangle in Figure 3c) and the
262 northeastern Pacific surface temperature (SST anomaly averaged over 30N-45N, 170 W-135W, red rectangle in
263 Figure 3c) have large signals in Figure 3c, and they were selected to show the extents to which SST or atmospheric
264 variation, which are connected to SST variation in the designated areas, can explain the changes in cloud and net
265 downward radiation flux.

266 To capture the dominant variations, spectrum analyses were conducted using normalized Nino3.4 SST and
267 northeastern Pacific SST, and Figure 7 shows the spectrum of SST when using both. Nino3.4 SST has a spectrum
268 peak at around five years, whereas the northeastern Pacific SST has a spectrum peak at 10 to 20 years. The former
269 corresponds to the ENSO period, and the latter corresponds to interdecadal variation in the mid-latitudes of the
270 Pacific, such as the PDO (Mantua et al. 1997). These results show that Nino3.4 SST and the northeastern Pacific
271 SST represent different variations over certain time scales, and the influence of both elements can be examined
272 through these indices.

273 In calculating the regression values with the area-averaged SST fluctuations (i.e., Nino3.4 SST or the
274 northeastern Pacific SST), we used the modified regression values defined in 2.3. Through this manipulation, it
275 was possible to determine how much of each physical quantity relating to variations in the Nino3.4 index,
276 equatorial Pacific SST, or northeastern Pacific SST (representing midlatitude variation), corresponded to the
277 variations in global mean surface temperature.

278 The patterns shown in both maps (Figure 8c, f) of the differences in the modified regression value of the
279 net downward radiation flux defined in the above equations (Eq (2-2) and Eq (2-3)) resemble those of the
280 differences in the regression values against global mean surface temperature (Figure 4b).

281 The areas showing large signals in the subtropics in the map of net downward radiation flux against global
282 mean surface temperature (Figure 4b) occur both in the northern Pacific (15N-32N, 170E-120W) and in the
283 southern Pacific (15S-30S, 160E-130W). Therefore, we calculated the regression value difference averaged over
284 those areas (blue and purple rectangles shown in Figure 8c, f). The modified regression value differences over
285 those areas were -1.73 and -2.14 [W/m^2] for the Nino3.4 index and -1.71 and -0.54 [W/m^2] for the northeastern
286 Pacific SST, respectively. However, the regression value differences against the global mean surface temperature
287 over those areas were -4.05 and -2.97 [W/m^2]. Therefore, the modified regression value differences were
288 approximately 42.7% and 72.1% for Nino3.4 SST and 42.3% and 18.1% for northeastern Pacific SST compared
289 to the global mean surface temperature.

290 In the same manner, the regression differences of surface temperature, sea level pressure (SLP), and the
291 mass content of cloud water were examined, with a focus on the connection between the net downward radiation

292 flux in the northern Pacific and Nino3.4 and northeastern Pacific SST variation. Figure 8a and 8d are maps of the
293 modified regression value differences of surface temperature and sea level pressure against Nino3.4 SST and the
294 Northeastern Pacific SST, respectively. The shape of the regression difference in surface temperature is long,
295 slender, and positive on the equatorial Pacific against Nino3.4 SST, whereas there is a wider positive regression
296 difference against the northeastern Pacific SST. Furthermore, their distributions in the northern Pacific are
297 completely different, which affirms that Nino3.4 SST and the northeastern Pacific SST represent different
298 variations both spatially and temporally.

299 With respect to SLP, the negative regression difference against northeastern Pacific SST in the northern
300 Pacific, which represents the strength and position of the Aleutian low, is located more closely to Alaska than
301 when using the Nino3.4 SST (Figure 8a, d). In addition, the positive regression difference against the northeastern
302 Pacific SST in the northwestern Pacific, which denotes anticyclonic circulation, extends more over the middle of
303 the Pacific compared to when using Nino3.4 SST. This SLP pattern strengthens the northern wind inflow, which
304 is supposed to lower the northeastern Pacific SST.

305 Figure 8b and 8e are maps showing the modified regression value differences of the mass cloud water
306 content against Nino3.4 SST and Northeastern Pacific SST, respectively. With respect to the cloud water content,
307 the regression value difference against northeastern Pacific SST is more positive in the northern subtropical Pacific
308 than when against Nino3.4 SST. This result can be attributed to the strengthening of the northern wind inflow,
309 which provides a more statically stable environment that is appropriate for increasing low cloud.

310

311 4. Summary and Discussion

312 This study used the PFP, a new feedback parameter, to investigate the changes in climate feedback due to
313 internal variations. Data from the MIROC6 piControl simulation, which is one of the main models in CMIP6, were
314 analyzed. The PFP was found to vary on interdecadal time scales, and its amplitude was comparable to that of the
315 DFP calculated in previous studies (Andrews et al. 2018) using the AGCM with observed SST as a boundary
316 condition. The results show that climate feedback intensity can be modulated greatly by internal variations.

317 Variations in PFP were found to be connected to the background field, and a positive surface temperature
318 anomaly in the eastern Pacific and a negative anomaly in the western Pacific were determined, which resulted in
319 a less tilted thermocline. This anomalous SST contrast in the equatorial Pacific agrees with the results of
320 Watanabe et al. (2021). As they focused on the SST trend pattern, the results indicate that recent SST trend
321 patterns in the equatorial Pacific, such as the hiatus, can be explained by internal variability. We also found that
322 annual changes in the globally averaged net downward radiation flux, which occurred in accordance with
323 background change, caused variations in the PFP.

324 To investigate the cause of changes in the global mean net downward radiation flux, regression analyses
325 were conducted against global mean surface temperature using the difference between PFP_large (PFP > 1.85
326 W/m², expressed as PFP_large) and PFP_small (PFP < 1.11 W/m², expressed as PFP_small). As the global mean
327 surface temperature rose, the surface temperature rise in the equatorial Pacific increased in PFP_large, owing to
328 enhancement of the ENSO amplitude. This pattern corresponds with that of ENSO determined in several studies,

329 which show that its amplitude increases when the east-west SST contrast as a background field is reduced
330 (Guilyardi et al. 2009; Kim et al. 2014; Cai et al. 2015). In addition, changes in the net downward radiation flux
331 values became increasingly positive in the northern part of the equator and increasingly negative in the equator
332 and subtropics in PFP_large. These distribution changes in the net downward radiation flux were found to
333 correspond well to those of clouds, when there was a low cloud increase in the subtropics and middle to high cloud
334 changes around the equator, which revealed that changes in the net downward radiation flux in these areas were
335 attributed to the amount and distribution of cloud. The low cloud increase in the subtropics (Figure 5a, 6c), where
336 descending flow prevails permanently (Figure 6a), is considered to be caused by an intensification of descending
337 flow and a possible decline in dry air entrainment due to the higher static stability (Bretherton 2015). The low
338 cloud increase (Figure 5a, 6c) is consistent with the results of a preceding study (Zhou et al. 2016) that focused on
339 the increasing trends in low cloud cover in the eastern Pacific in correspondence with SST trend patterns, rather
340 than increasing anomalies in the subtropics.

341 These variational characteristics were derived as a superposition of multiple time- and special-scale
342 fluctuations. To evaluate the fluctuations that were dominant in controlling PFP variations, a modified regression
343 value was defined against Nino3.4 SST (SST anomaly averaged over 5S-5N, 170 W-120W, blue rectangle in
344 Figure 3c, which has a spectrum peak in near 5 years as shown in Figure 7) and Northeastern Pacific SST (SST
345 anomaly averaged over 30N-45N, 170 W-135W, red rectangle in Figure 3c, which has a spectrum peak in the later
346 10 years in Fig 7). This revealed that the low cloud increase and consequent changes in net downward radiation
347 flux in the southern Pacific were mainly attributed to changes in ENSO, as represented by the modified regression
348 value against Nino3.4 SST, whereas that in the northern Pacific was contributed to both by changes in ENSO and
349 longer changes in fluctuations (such as the PDO) in the northern mid-latitudes, which strengthened the static
350 stability of the subtropics. Since northeastern Pacific SST is located at higher latitudes than the subtropics, it is
351 anticipated that the increase in cloud water in the northern subtropics is not brought directly by the northeastern
352 Pacific SST, but through atmospheric circulation change over longer time scales, which can also control the
353 northeastern Pacific SST.

354
355 It has been suggested that variations in DFP are affected by lower cloud increases in the eastern Pacific in
356 relation to changes in SST trend patterns, active convection in the western Pacific, and the enhancement of static
357 stability in the boundary layer due to atmospheric heating in the middle-upper layer (Gregory and Andrews
358 2016; Zhou et al. 2016). The results of this study also indicate that increases in lower clouds and the subsequent
359 increase in reflection have a great impact on the radiation budget at the top of the atmosphere; however, this
360 occurs in the subtropical Pacific and is caused by multiple internal fluctuation changes.

361 The study of Shioyama et al. (2012) also showed that cloud negative feedback due to ENSO was intensified
362 when using a perturbed physics ensemble in MIROC5, and that of Toniazzo et al. (2008) achieved similar results
363 with the GCM of the Hadley Centre. Differences in the background features may thus influence the detailed
364 mechanisms working as negative feedback, and in this study we indicated that the zonal SST contrast along the
365 equator in the background was reduced due to global warming.

366 Fluctuations in the northeastern Pacific, defined by the northeastern Pacific SST in this study, involve
367 decadal to interdecadal variations, such as that of the PDO. A change in the strength of the Aleutian low is known
368 to be one of the drivers of this change (Newman et al. 2016). From this, variation changes or extreme position
369 shifts of sea level pressure in the northern Pacific can be caused by teleconnection pattern changes, such as the
370 NPO (Wallace and Gutzler 1981), which is from the equatorial Pacific (to the northern Pacific), and the PJ pattern
371 (Nitta 1987), which is from the maritime continent, and thus decadal fluctuations occur in the northern Pacific.
372 However, for teleconnection pattern changes, the influence of the background fields of the atmosphere cannot be
373 neglected.

374 Teleconnection differences and their mechanisms associated with background changes are currently being
375 studied. Michel et al. (2020) showed that many studies have suggested that the maximum region of SLP variation
376 has shifted toward the northeast (Christensen et al., 2007; Muller and Roeckner, 2008; Christensen and Coauthors,
377 2013). Other studies have provided contrasting results and suggested that the SLP anomaly has become larger
378 without changing its position (Schneider et al. 2009), has become weaker (Herceg et al. 2007), or has shifted
379 towards a westward direction (Zhou et al. 2014). One of reasons for such inconsistencies is the lack of a coherent
380 modeling span or ensemble size used in the different studies, and this has caused non-negligible differences in the
381 background field due to phase disagreements associated with internal variation (Michel et al., 2020).

382 Thus, elucidating air-sea interactions between the tropics and the extra tropics through large ensemble
383 simulations and multi-model analyses will contribute to improving the evaluation of climate feedback.

384

385 **Abbreviations**

386 CS, climate sensitivity; ECS, equilibrium climate sensitivity; GCM, general circulation model; AR1: 1st
387 assessment report; AR5: 5th assessment report; EffCS, effective climate sensitivity; DFP, differential feedback
388 parameter; AGCM, atmospheric general circulation model; SST, sea surface temperature

389

390 **Declarations**

391

392 **Acknowledgements**

393 The MIROC6 dataset supporting the conclusions of this article is available from [https://esgf-](https://esgf-node.llnl.gov/search/cmip6/)
394 [node.llnl.gov/search/cmip6/](https://esgf-node.llnl.gov/search/cmip6/).

395 This work was supported by JSPS KAKENHI Grant Number JP19H05703 and by the Integrated Research
396 Program for Advancing Climate Models (Tougo) Grant Numbers JPMXD0717935457 and JPMXD0717935715.

397

398 **Author contributions**

399 Ko Tsuchida: Conceptualization; data analysis and investigation; writing (and original draft).

400 Takashi Mochizuki: Funding acquisition, resources, supervision, writing, review, and editing.

401 Ryuichi Kawamura and Tetsuya Kawano: Discussion and advice.

402

403 **References**

404

405 Andrews T, Gregory JM, Mark et al. (2012) Forcing, feedbacks and climate sensitivity in CMIP5 coupled
406 atmosphere-ocean climate models. *Geophys Res Lett* 39:L09712. doi:[10.1029/2012GL051607](https://doi.org/10.1029/2012GL051607)

407

408 Andrews T, Gregory JM, Paynter DSilvers, L. G., Zhou, C., Mauritsen, T., et al. (2018): Accounting for changing
409 temperature patterns increases historical estimates of climate sensitivity. *Geophys. Res. Lett.*, **45**, 8490–8499

410

411 Arakawa, A. and Konor, C. S. (1996): Vertical differencing of the primitive equations based on the Charney-
412 Phillips grid in hybrid σ - p vertical coordinates, *Mon. Weather Rev.*, 124, 511–528.

413

414 Bony S, Colman R, Kattsov VM et al. (2006) “How well do we understand and evaluate climate change feedback
415 processes?” *J Clim* 19:3445–3482

416

417 Bretherton CS. (2015): Insights into low-latitude cloud feedbacks from high resolution models. *Phil. Trans. R.*
418 *Soc. A* 373: 20140415. <http://dx.doi.org/10.1098/rsta.2014.0415>

419

420 Cai, W., Santoso, A., Wang, G. et al. (2015): ENSO and greenhouse warming. *Nature Clim Change* 5, 849–859.
421 <https://doi.org/10.1038/nclimate2743>

422

423 Christensen and Coauthors (2013): Climate phenomena and their relevance for future regional climate change.
424 *Climate Change (2013): The Physical Science Basis*, T. F. Stocker et al., Eds., Cambridge University Press,
425 1217–1308.

426

427 Forster PMF, Gregory JM (2006) The climate sensitivity and its components diagnosed from earth radiation budget
428 data. *J Clim* 19:39–52. DOI: <https://doi.org/10.1175/JCLI3611.1>

429

430 Gregory J, Webb M (2008) Tropospheric adjustment induces a cloud component in CO₂ forcing. *J Clim* 21:58–
431 71

432

433 Gregory JM, Andrews T (2016) Variation in climate sensitivity and feedback parameters during the historical
434 period. *Geophys Res Lett* 43:3911–3920. doi:[10.1002/2016GL068406](https://doi.org/10.1002/2016GL068406)

435

436 Gregory JM, Andrews T, Ceppi P et al. (2020) How accurately can the climate sensitivity to CO₂ be estimated
437 from historical climate change? *Clim Dyn* 54:129–157. <https://doi.org/10.1007/s00382-019-04991-y>

438

439 Gregory JM, Ingram WJ, Palmer MA, Jones GS et al. (2004) A new method for diagnosing radiative forcing and

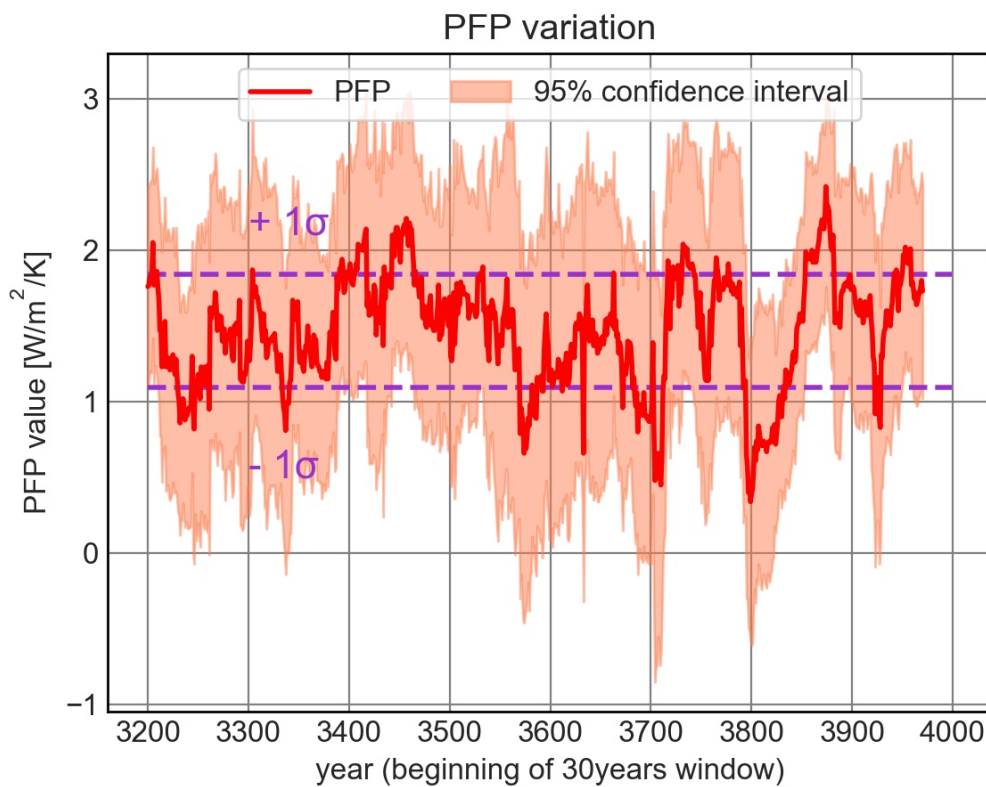
440 climate sensitivity. *Geophys Res Lett* 31:L03205. doi:[10.1029/2003GL018747](https://doi.org/10.1029/2003GL018747)
441
442 Gregory JM, Stouffer RJ, Raper SCB et al. (2002) An observationally based estimate of the climate sensitivity. *J*
443 *Climate* 15:3117–3121
444
445 Guilyardi, E., Wittenberg, A., Fedorov, A., Collins, M., Wang, C., Capotondi, A., et al. (2009): Understanding El
446 Niño in ocean-atmosphere general circulation models: Progress and Challenges *Bull. Amer. Meteor. Soc.*, 90,
447 325–340. <https://doi.org/10.1175/2010JCLI3679.1>.
448
449 Herceg Bulić, I., and C. Branković (2007): ENSO forcing of the Northern Hemisphere climate in a large
450 ensemble of model simulations based on a very long SST record. *Climate Dyn.*, 28, 231–254, [https://doi.org](https://doi.org/10.1007/s00382-006-0181-1)
451 [/10.1007/s00382-006-0181-1](https://doi.org/10.1007/s00382-006-0181-1).
452
453 Kim et al. (2014): Response of El Niño sea surface temperature variability to greenhouse warming. *Nature Clim.*
454 *Change* 4, 786-790.
455
456 Knutti R, Hegerl GC (2008) The equilibrium sensitivity of the Earth’s temperature to radiation changes. *Nat Geosci*
457 1:735–743. <https://doi.org/10.1038/ngeo337>
458
459 Mantua et al. (1997) : A Pacific Interdecadal Climate Oscillation with Impacts on Salmon Production; *Bull.*
460 *Amer. Meteor. Soc.*, Vol.78, pp.1069-1079.
461
462 Meehl and Teng (2007): Multi-model changes in El Niño teleconnections over North America in a future
463 warmer climate. *Clim Dyn* 29, 779–790. <https://doi.org/10.1007/s00382-007-0268-3>.
464
465 Michel, C., C. Li, I. R. Simpson, et al. (2020): The Change in the ENSO Teleconnection under a Low Global
466 Warming Scenario and
467 the Uncertainty due to Internal Variability. *J. Clim*, 33, 4871–4889,
468 <https://doi.org/10.1175/JCLI-D-19-0730.1>.
469
470 Müller and Roeckner (2008): ENSO teleconnections in projections of future climate in ECHAM5/MPI-OM. *Clim*
471 *Dyn* 31, 533–549. <https://doi.org/10.1007/s00382-007-0357-3>.
472
473 Newman et al. (2016): The Pacific Decadal Oscillation, revisited. *J. Clim.* 29, 4399–4427.
474
475 Nitta (1987): Convective activities in the tropical western Pacific and their impact on the northern hemisphere
476 summer circulation. *J. Meteor. Soc. Japan*, 78. 141-157.

477
478 Otto A, Otto FEL, Boucher O et al. (2013) Energy budget constraints on climate response. *Nat Geosci* 6:415–416.
479 <https://doi.org/10.1038/ngeo1836>
480
481 Power et al. (1999) : Inter-decadal modulation of the impact of ENSO on Australia; *Clim. Dyn.*, 15, pp.319-324.
482
483 Schneider et al. (2009): A statistical-dynamical estimate of winter ENSO teleconnections in a future climate. *J.*
484 *Clim*, 22, 6624–6638, <https://doi.org/10.1175/2009JCLI3147.1>.
485
486 Senior CA, Mitchell JFB (2000) The time-dependence of climate sensitivity. *Geophys Res Lett* 27:2685–2688
487
488 Shiogama, H., Watanabe et al. (2012): Perturbed physics ensemble using the MIROC5 coupled atmosphere–
489 ocean GCM without flux corrections: experimental design and results. *Clim Dyn* 39, 3041–3056.
490 <https://doi.org/10.1007/s00382-012-1441-x>
491
492 Tett SFB, Betts R, Crowley TJ et al. (2006) The impact of natural and anthropogenic forcings on climate and
493 hydrology since 1550. *Clim Dyn* 28:3–34. <https://doi.org/10.1007/s00382-006-0165-1>
494 <https://doi.org/10.1029/2018GL078887>
495
496 Tatebe, H., Ogura, T., Nitta, T., Komuro, et al. (2013): Description and basic evaluation of simulated mean state,
497 internal variability, and climate sensitivity in MIROC6, *Geosci. Model Dev.*, 12, 2727–2765,
498 <https://doi.org/10.5194/gmd-12-2727-2019>.
499
500 Toniazzo and Woolnough (2014): Development of warm SST errors in the southern tropical Atlantic in CMIP5
501 decadal hindcasts. *Clim Dyn* 43, 2889–2913. <https://doi.org/10.1007/s00382-013-1691-2>.
502
503 Wallace and Gutzler (1981): Teleconnections in the geopotential height field during the Northern Hemisphere.
504 *Mon. Wea. Rev.*, 109, 784–812, [https://doi.org/10.1175/15200493\(1981\)109,0784:TITGHF.2.0.CO;2](https://doi.org/10.1175/15200493(1981)109<0784:TITGHF.2.0.CO;2).
505
506 Wang et al. (2013) : Northern Hemisphere summer monsoon intensified by mega-El Niño/southern oscillation and
507 Atlantic multidecadal oscillation; *Proc Natl Acad Sci USA*, Vol.110, No.14, pp.5347-5352.
508
509 Watanabe, M., Dufresne, JL., Kosaka, Y., et al. (2021) Enhanced warming constrained by past trends in
510 equatorial Pacific sea surface temperature gradient. *Nat. Clim. Chang.* **11**, 33–37.
511 <https://doi.org/10.1038/s41558-020-00933-3>.
512
513 Zhang et al. (1997) : ENSO-like Interdecadal Variability: 1900–93; *J. Climate*, Vol.10, pp.1004-1020.

514
515
516
517
518
519
520
521
522
523
524
525
526
527
528
529

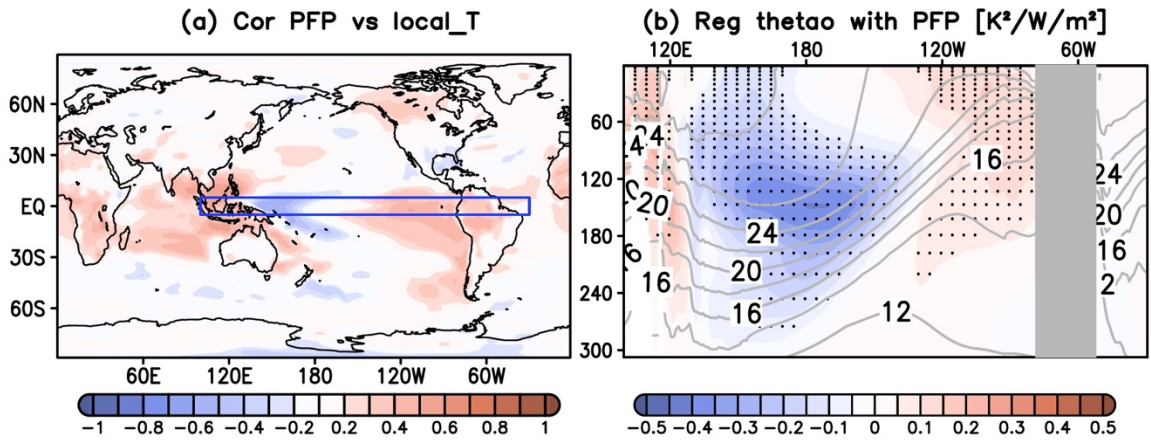
Zhou et al. (2014): Global warming induced changes in El Niño teleconnections over the North Pacific and North America. *J. Clim.*, 27, 9050–9064, <https://doi.org/10.1175/JCLI-D-14-00254.1>.

Figure legends



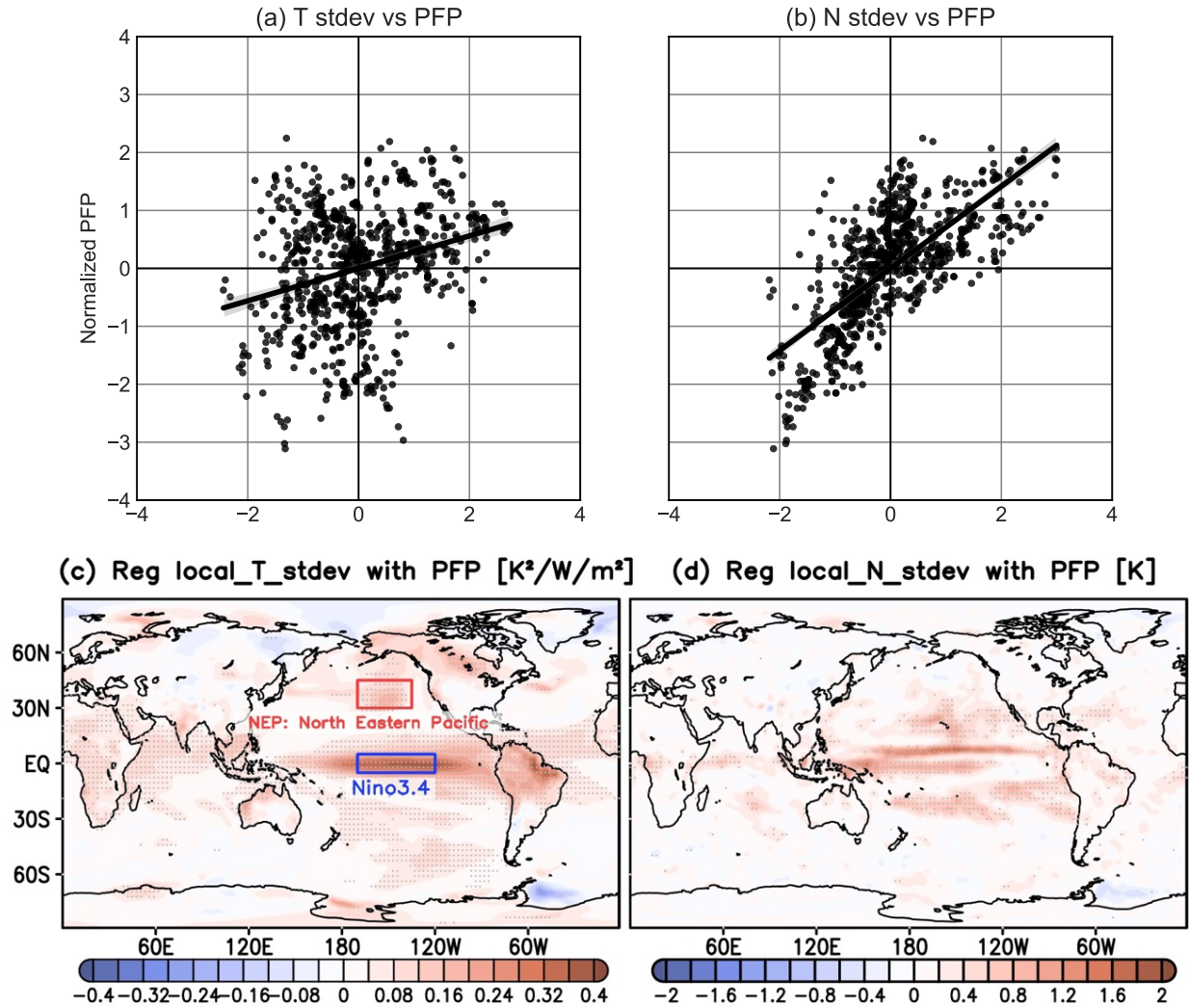
530
531
532

Figure 1. PFP time series (red line) and ranges over the 95% confidence level (orange shading) derived using the t-test. Purple lines indicate a range of ± 1 standard deviation from the PFP mean value.

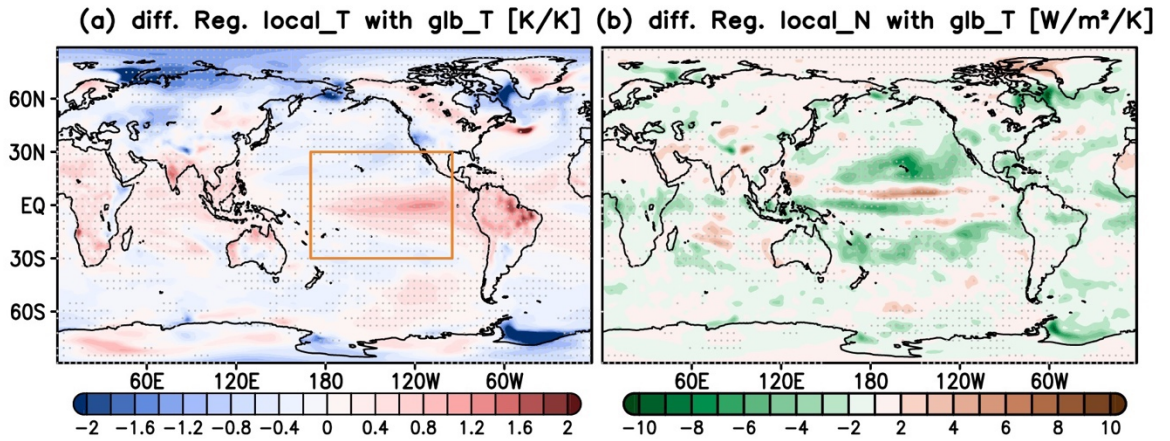


533
 534
 535
 536
 537
 538

Figure 2.(a) Map showing correlation between 30-year running mean surface temperature and PFP. (b) Longitude-depth section of 30-year running mean ocean-temperature averaged meridionally over the blue rectangle shown in panel (a) regressed onto PFP. Contours in panel (b) show ocean-water temperature averaged over 800 years. Stippling in panel (b) indicates that the regression value is significant at a 95% confidence level (derived using the t-test technique).

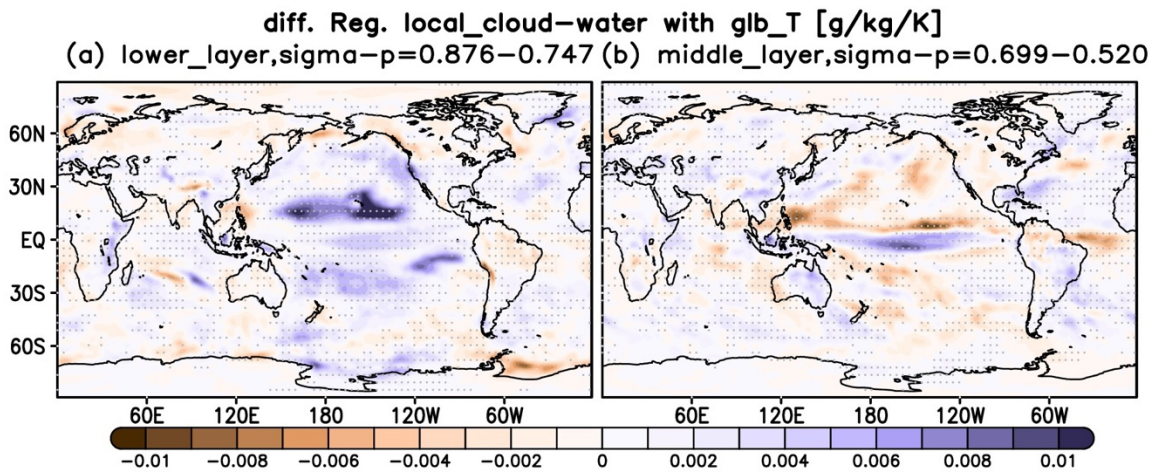


539 Figure 3. (Upper panels) Scatter plot of normalized PFP against normalized standard deviation of global
 540 means of (a) surface temperature and (b) net downward radiation flux at TOA respectively in 30 years. Lines
 541 in panels (a) and (b) show the slope of the ordinary least squares (OLS) regression of normalized PFP against
 542 the normalized standard deviation of global mean surface temperature and net downward radiation flux at
 543 TOA, respectively, in 30 years. (Lower panels) Standard deviations of (c) surface temperature and (d) net
 544 downward radiation flux at TOA in 30 years regressed to PFP. Stippling in panels (c) and (d) indicate the
 545 areas where the regression value is significant at a 95% confidence level derived by t-test technique.



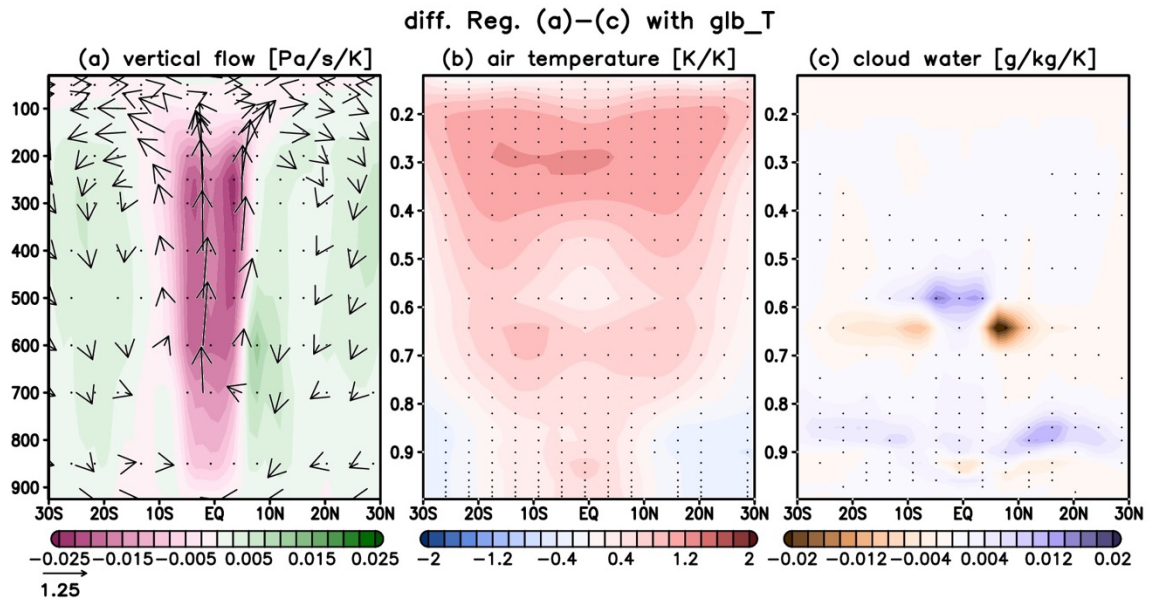
546
547
548
549
550
551

Figure 4. Maps showing differences between PFP_large and PFP_small when (a) surface temperature and (b) net downward radiation flux were regressed onto global mean surface temperature. Stippling indicates the areas where the regression value is significant at a 99% confidence level (derived using the t-test technique). Orange rectangle in panel (a) is the analyzed area in Figure 6.



552
553
554
555

Figure 5. The same as in Figure 4, except for cloud water contents averaged over the levels of (a) 0.876–0.747 and (b) 0.699–0.520 using the hybrid $\sigma - p$ coordinate.



556

557

558

559

560

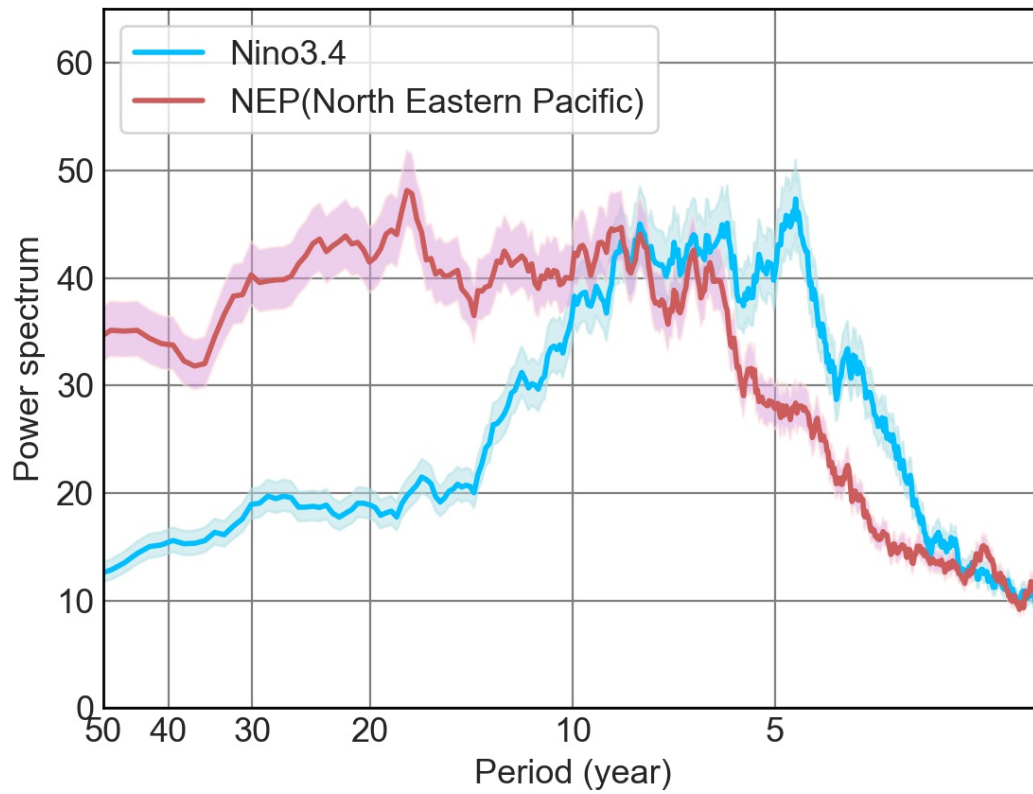
561

562

563

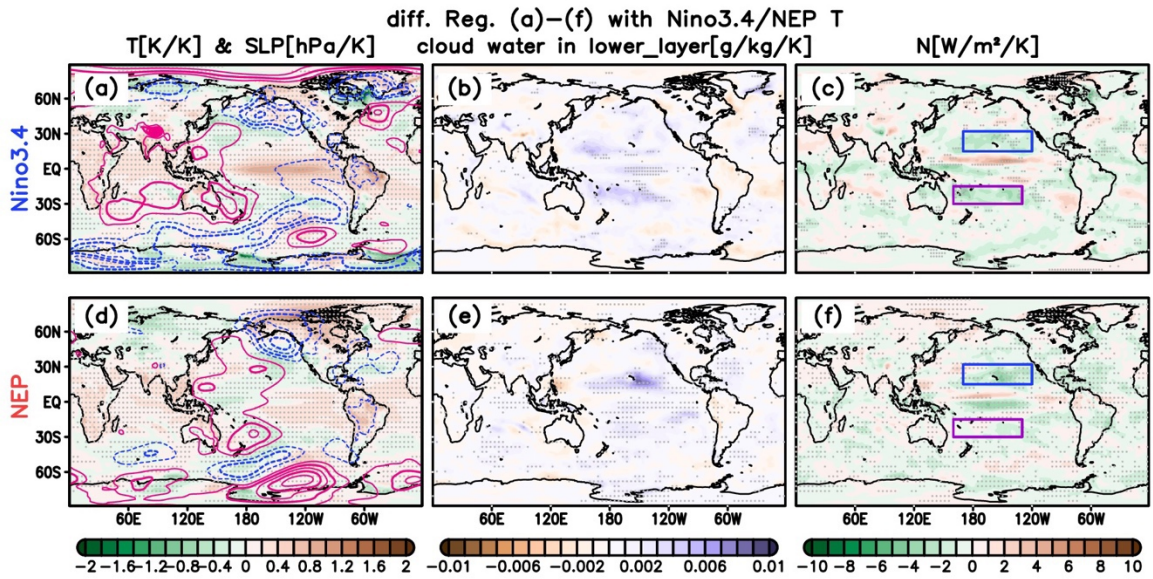
564

Figure 6. Differences between PFP_large and PFP_small for (a) vertical winds (shading) and meridional circulation winds (vector), (b) air temperature, and (c) cloud water content, zonally averaged over the area shown in Figure 4 (orange rectangle) and regressed onto global mean surface temperature. The vertical components of the vectors in (a) are multiplied by a factor of 100. The vertical coordinate in (b) and (c) is depicted by the hybrid $\sigma - p$ coordinate. The stippling indicates the 99% confidence level (derived using the t-test technique).



565
 566
 567
 568
 569
 570
 571
 572
 573

Figure 7. Power spectrums of surface temperature variations averaged over Nino3.4 (blue solid line) and the NEP area (red solid line) designated in Figure 3. Plotted values are smoothed using 30-point running means. Shadings indicate the ranges over 99% confidence level (derived using the t-test technique).



574
 575
 576
 577
 578
 579
 580
 581
 582
 583
 584
 585
 586
 587

Figure 8. (a) Map of the modified regression value differences between PFP_large and PFP_small of surface temperature and sea level pressure against Nino3.4 SST. Modified regressions of differences to surface temperature averaged over Nino3.4 area, in surface temperature (shading) and sea level pressure (contour, 0.3 hPa/K interval). Stippling indicates 99% confidence level (derived using the t-test technique). (b) The same as in panel (a), except for the cloud water content in the lower_layer (same definition mentioned in Figure 5(a)). (c) The same as in panel (a), except for the net downward radiation flux at top-of-atmosphere. The blue and purple rectangles were used in the regression analysis (see text 4.3 in detail). (d, e, f) The same as in panels (a, b and c) except for the regression values against surface temperature averaged over the NEP area.